PERGAMON

International Journal of Heat and Mass Transfer 42 (1999) 1075–1095

International Journal of
HEAT and MASS
TRANSFER

Role of inter- and intraparticle diffusion in nonuniform particle size gasless compacted powder combustion synthesis—II: results and comparison with experiment

A. A. M. Oliveira, M. Kaviany*

Department of Mechanical Engineering and Applied Mechanics, The University of Michigan, 2250 G. G. Brown, Ann Arbor, MI 48109-2125, U.S.A.

Received 20 December 1996; in final form 7 April 1998

Abstract

Following Part I, the predicted results of a combined three-scale, specimen-level/particle-level treatment of gasless, combustion synthesis of intermetallics, for a system with specimen-level composition corresponding to $TiAl_3$, is presented. It is shown that the intraparticle diffusion, modeled by a high reaction rate (i.e., primary-diffusion) regime followed by a lower reaction rate (i.e., secondary-diffusion) regime, determines the front structure and the propagation speed. The nonuniform particle-size distribution limits the availability of the reactants at a particle level, thus determining the extent of conversion to the final product and the maximum temperature. Experiments are performed for the aluminium–titanium system for two different titanium (higher melting temperature reactant) powder sizes. The model predicts a lower conversion than that observed in the experiments, indicating the importance of interparticle diffusion. There is good agreement between the predicted and measured variations of propagation speed and maximum temperature with respect to the average particle size. © 1998 Elsevier Science Ltd. All rights reserved.

Nomenclature

A_{sa} specimen peripheral area [m^2]
c_p specific heat capacity [$J\ kg^{-1}\ K^{-1}$]
b shape parameter
D diameter [m]
D_{A-C} binary diffusivity of species A [$m^2\ s^{-1}$]
D_o diffusion pre-exponential factor [$m^2\ s^{-1}$]
f particle size distribution function
F_c conversion fraction
F_l liquid fraction
h_{sa} heat transfer coefficient between specimen and ambient [$W\ m^{-2}\ K^{-1}$]
i specific enthalpy [$J\ kg^{-1}$]
$\langle k \rangle$ effective molecular thermal conductivity [$W\ m^{-1}\ K^{-1}$]
$\langle k_r \rangle$ effective radiant thermal conductivity [$W\ m^{-1}\ K^{-1}$]
l unit-cell characteristic length [m]
M molecular weight [$kg\ kmol^{-1}$]
N number of classes in the discrete particle size distribution function
$\dot{n}_{ls}$ volumetric melting rate [$kg\ m^{-3}\ s^{-1}$]
$\dot{n}_r$ volumetric reaction rate [$kg\ m^{-3}\ s^{-1}$]
r radial coordinate [m]
R radius [m]
R_g universal gas constant [$J\ kmol^{-1}\ K^{-1}$]
t time [s]
T temperature [K]
u velocity [$m\ s^{-1}$]
V volume of unit cell [m^3]
V_s volume of specimen [m^3]
x axial coordinate [m]
Y mass fraction.

Greek symbols

$\Delta E_{a,D}$ diffusion activation energy [$J\ kmol^{-1}$]
Δi_r specific heat of combustion [$J\ kg^{-1}$]
Δi_{ls} specific heat of melting [$J\ kg^{-1}$]
Δi_m specific heat of mixing [$J\ kg^{-1}$]

---

* Corresponding author. Tel.: 001 734 936 0402; fax: 001 734 647 3170; e-mail: kaviany@umich.edu

0017–9310/98 $19.00 © 1998 Elsevier Science Ltd. All rights reserved
PII: S0017-9310(98)00158-6

δ	thickness [m]
ε	porosity
ν	number of moles [kmol]
ρ	density, mass concentration [kg m^{-3}]
θ	scale parameter [m].

Subscripts

a	ambient
ad	adiabatic
A	species A
B	species B
c	converted
C	species C
e	effective
f	formation
F	combustion front
g	gas phase
i	species i, subunit cell
l	liquid-phase
m	mixture
n	nonreacted
r	reaction, reacted, radiation or radial
s	solid phase, specimen
sa	between specimen and ambient
tran	transition from the primary-diffusion regime to the secondary-diffusion regime
1	transformed coordinate.

Superscripts

A–C	diffusion layer
o	standard state (pure component).

Other symbols

—	ensemble average
$\langle\ \rangle$	local volume-averaged
$\langle\ \rangle^i$	local phase-volume averaged.

1. Introduction

The model developed in Part I for the treatment of the gasless combustion synthesis [1], is now applied to the aluminium–titanium system with specimen-level composition corresponding to $TiAl_3$ and the predictions are verified experimentally.

The adiabatic equilibrium temperature, determined for the specimen-level stoichiometric condition and by using the heat of formation from [7], is 1647 K (the melting temperature of $TiAl_3$) and 30% of liquid product should be formed. Sohn and Wang [2] and Wright and Rabin [3] observed temperature distributions with a maximum temperature around 1510 K. However, Hanamura [4], conducting tests with a narrow range size-distribution of fine powders, reports that the maximum temperature approaches the reported melting temperature of $TiAl_3$ (1647 K) and is basically independent of the initial temperature. Our own experiments confirm these results and from BSEM pictures taken from the reacted samples, there is evidence of non-converted reactants, both as a titanium-rich core and as an aluminium-rich layer covering the surface of the particles. This appears to be caused by the simultaneous effects of the heat losses, nonuniform distribution of melted aluminium around the titanium particles and the delayed diffusion through the larger titanium particles.

The objective here is to predict the extent of conversion to the final product as well as the characteristics of the combustion front (i.e., the propagation speed and the maximum temperature) as a function of the particle statistics (average radius, standard deviation and skewness). Comparison is made with the simpler premixed-type combustion models and the effect of the phase change is analyzed for systems that present an appreciable melting of products.

In the following, initially, the powders are characterized, the experimental procedure is shortly described and the experimental results are presented. Then the thermophysical properties and the solution of the conservation equations are briefly discussed. The predictions of the model developed in Part I are then compared with the experiments and the roles of the particle-size distribution, intraparticle diffusion, phase change, and average particle size are discussed.

2. Experiment

Experiments are performed for the Al–Ti system in the specimen-level composition corresponding to $TiAl_3$. This compound was chosen because of its technological importance [5], its relatively simple phase diagram and because the adiabatic equilibrium temperature is below the melting point of one of the components (titanium). Aluminium and titanium powders 99.5% pure were obtained from CERAC Inc. and Alfa AESAR (Johnson–Matthey). The aluminium powder is 325 MESH and for the titanium, a 325 MESH powder and a powder with nominal diameter ranging from 1 to 3 μm are used. Although the aluminium particles can be characterized as round, the titanium particles are highly irregular.

The maximum and minimum lengths of particles sampled from the powders are measured from electron micrographs. A total of 155 particles were measured for the 325 MESH powder and 407 particles for the 1–3μm powder. Since the number of particles sampled is relatively small the uncertainty in the values of f related to the sample size is estimated to be smaller than 10%. The equivalent-sphere radius (based on the analysis in Part I) is calculated for both the titanium and aluminium particles. Figure 1 presents the distribution functions (number densities) for the titanium powders. The particle size dis-

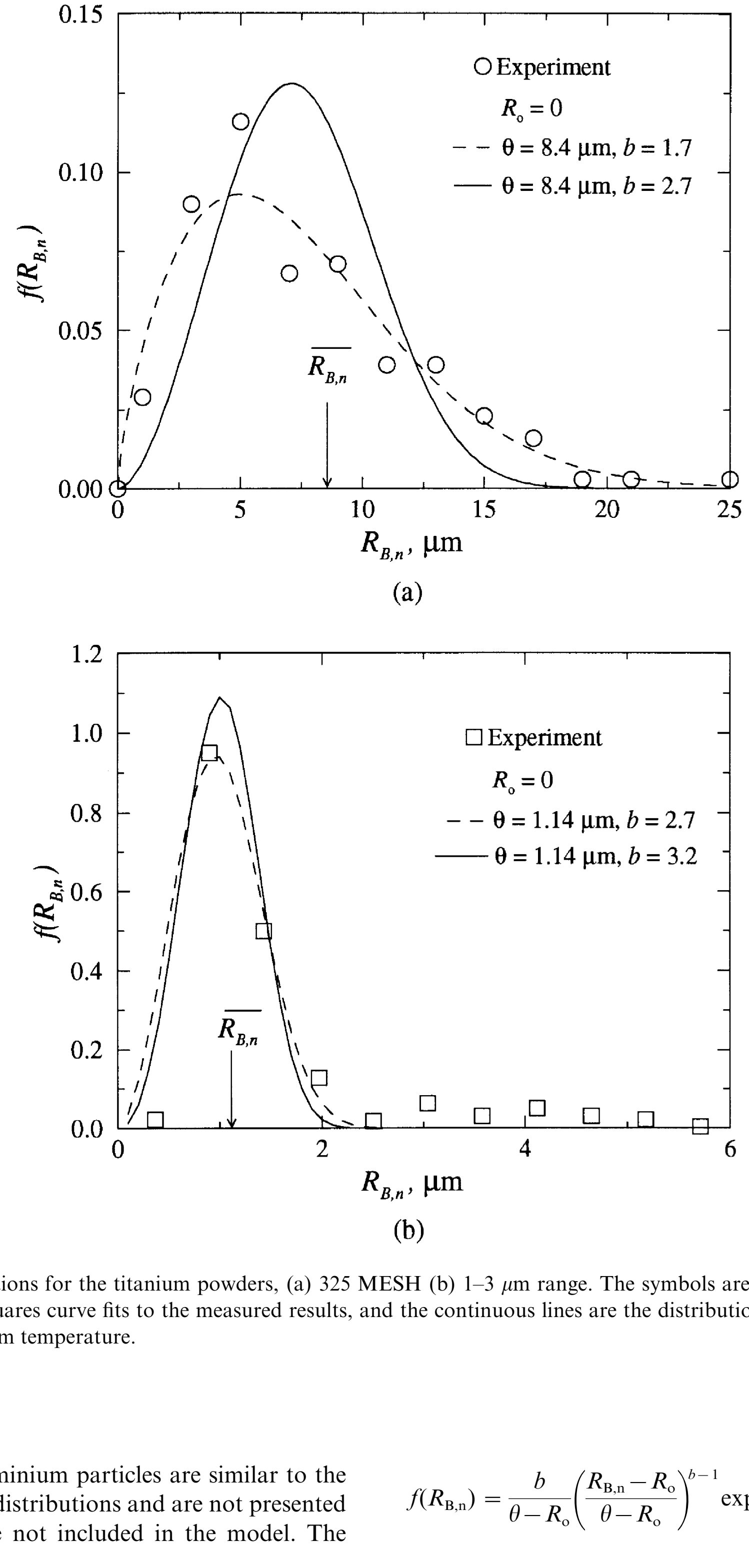

Fig. 1. Particle-size functions for the titanium powders, (a) 325 MESH (b) 1–3 μm range. The symbols are the measured results, the dashed lines are least-squares curve fits to the measured results, and the continuous lines are the distribution function corresponding to the measured maximum temperature.

tributions for the aluminium particles are similar to the titanium particle-size distributions and are not presented here because they are not included in the model. The Weibull distribution [6] is used here to characterize the particle-size distribution. In its most general form it is given by

$$f(R_{\rm B,n}) = \frac{b}{\theta - R_{\rm o}}\left(\frac{R_{\rm B,n}-R_{\rm o}}{\theta - R_{\rm o}}\right)^{b-1}\exp\left(-\left(\frac{R_{\rm B,n}-R_{\rm o}}{\theta - R_{\rm o}}\right)^{b}\right), \tag{1}$$

where $R_{\rm o}$ is the cut-off radius and θ and b are the scale and shape parameters.

The curve fitting of the Weibull distribution to the measured particle size distribution functions, assuming $R_o = 0$ μm, resulted in $b = 1.7$ and $\theta = 8.4$ μm for the 325 MESH and $b = 2.7$ and $\theta = 1.14$ μm for the 1–3 μm powders (Fig. 1).

The specimens preparation consists of mixing the powders, manual filling of the rubber molds and cold isostatic pressing at 134 MPa for the coarser and 235 MPa for the finer powders. The molds have holes in the walls that allow for the positioning of the thermocouples before the pressing. AWG 32 bare wires (0.008 in = 0.2019 mm) platinum/platinum + 13% rhodium (type R) thermocouples coated with silica (using hexamethyldisiloxane) are used. In the non-reacted state, the samples for the coarser powder presented an average porosity of 0.3 and diameter of 1.1 cm while for the finer powder, the porosity was 0.2 and the diameter was 1.0 cm. The initial length was about 9.5 cm. The thermocouples are located, from the top of the specimens, at 3, 5 and 7 cm locations.

Figure 2 presents a sketch of the experimental setup. The specimens, placed on top of a stainless steel tube, are preheated by a cylindrical electric heater made of alumina with an embedded electrical resistor. The specimen can be filmed through a quartz window placed on the heater wall. The ignition is by a small ignition specimen positioned on the top of the test specimen. Aluminium foil is placed between the two specimens to enhance the thermal contact after melting of the foil. The small specimen is ignited using a premixed propane–air torch. An automatic data acquisition system is used to record the temperature.

Figure 3(a)–(c) show the combustion front propagating through a short specimen (for which the heater was removed after ignition). Note that during combustion there is a swelling of the specimen, but it does not lose its structural stability.

Figure 4 shows the time variation of the temperature as recorded by the three thermocouples in Tests 3 and 4. For Test 3, the preheating (non-reacted region) temperature is 600°C and the aluminium melting plateau at 650°C is clearly visible in the temperature evolution for

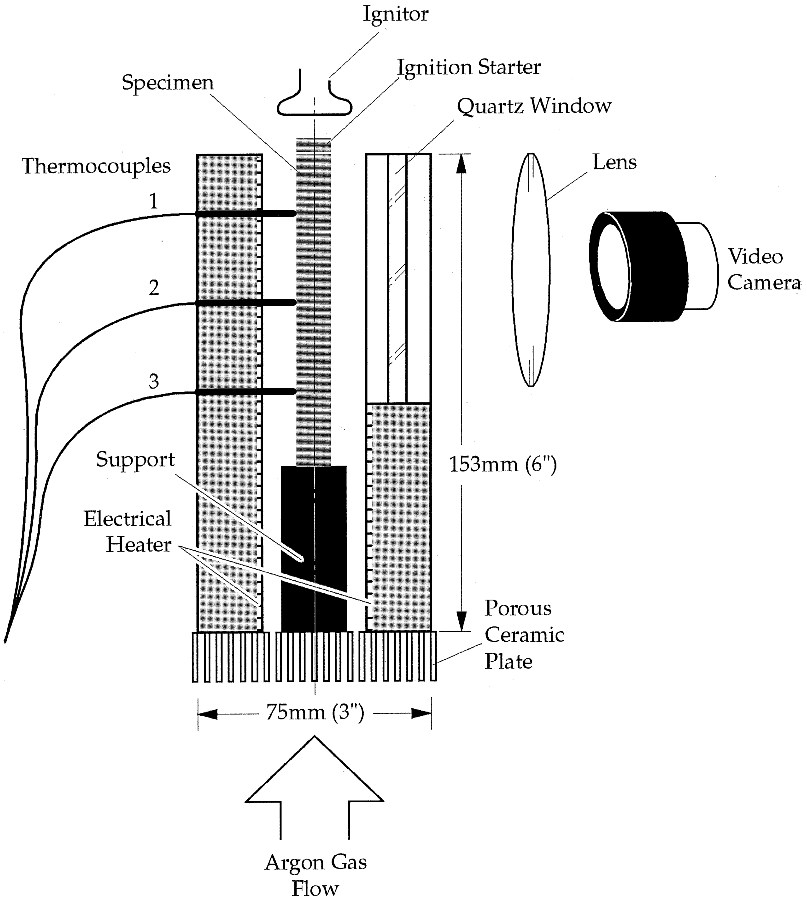

Fig. 2. Experimental setup, showing the specimen, the thermocouple locations, the ignition sample and the inert-gas flow.

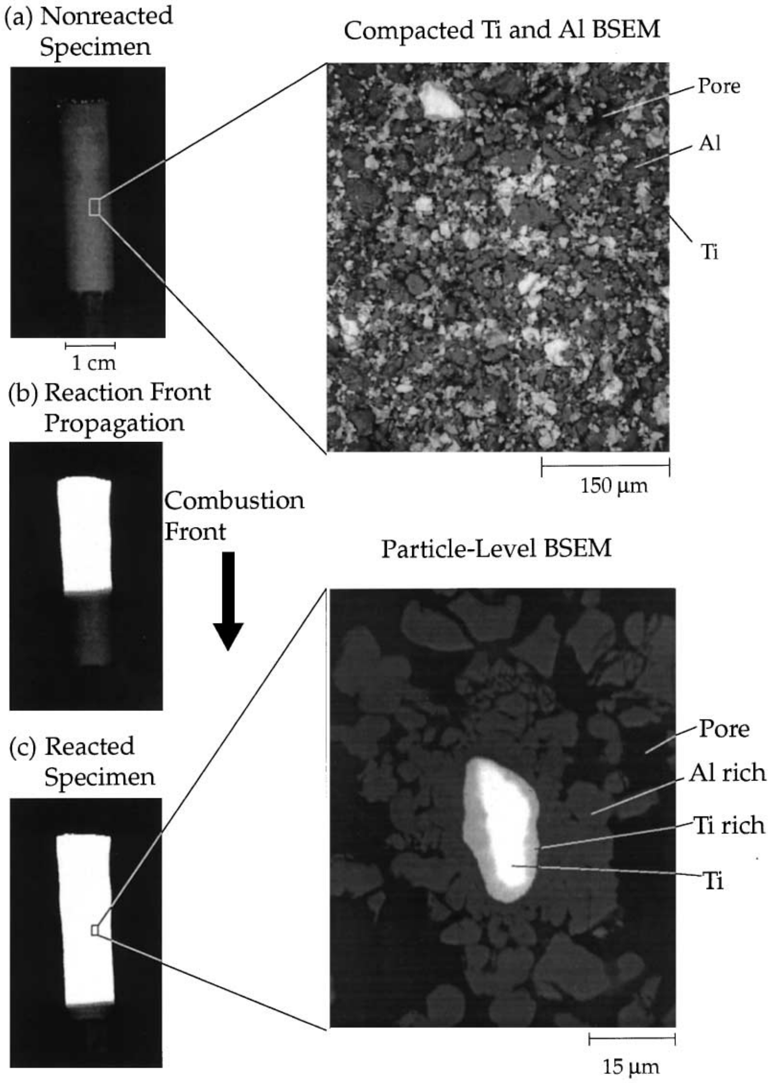

Fig. 3. Combustion front propagating through a short sample and back-scattered electron micrographs (BSEM) of the nonreacted compacted powder and the reacted specimen.

thermocouple 1. The ignition has a smaller effect in the location of thermocouple 3 and the melting of aluminium plateau is no longer visible. For Test 4, the preheating of the specimen is not as homogeneous as in Test 3 and the melting of aluminium is not visible for both thermocouples 2 and 3. Note also that, although there is a variation of 100 K in the preheating temperature, the maximum temperature is approximately constant. The uncertainty in the temperature measurement is estimated to be $\pm 10^\circ$C at the maximum temperature. Temperature profiles similar to the ones for Test 3 have been measured by others [2, 3].

Table 1 presents the test results. In Table 1, $T_{r,1}$, $T_{r,2}$, and $T_{r,3}$ are, respectively, the maximum temperatures recorded by thermocouples 1, 2, and 3 (numbered from the top). The front speed $u_{F,v}$ is from the analysis of the video recording based on the time of travel of the combustion wave between two neighboring points (marked references) around the location of the thermocouple 2. The other two front speeds reported in Table 1 are obtained from the transient temperature distributions, $u_{F,1\text{–}2}$ is based on the time of travel between the locations of thermocouples 1 and 2, and $u_{F,2\text{–}3}$ is based on thermocouples 2 and 3. After combustion (reacted state), the samples for the coarser powder have porosity 0.45 and diameter of 1.2 cm while for the finer powder, the porosity is about 0.3 and the diameter about 1.1 cm. The final length varied from 10 to 11 cm.

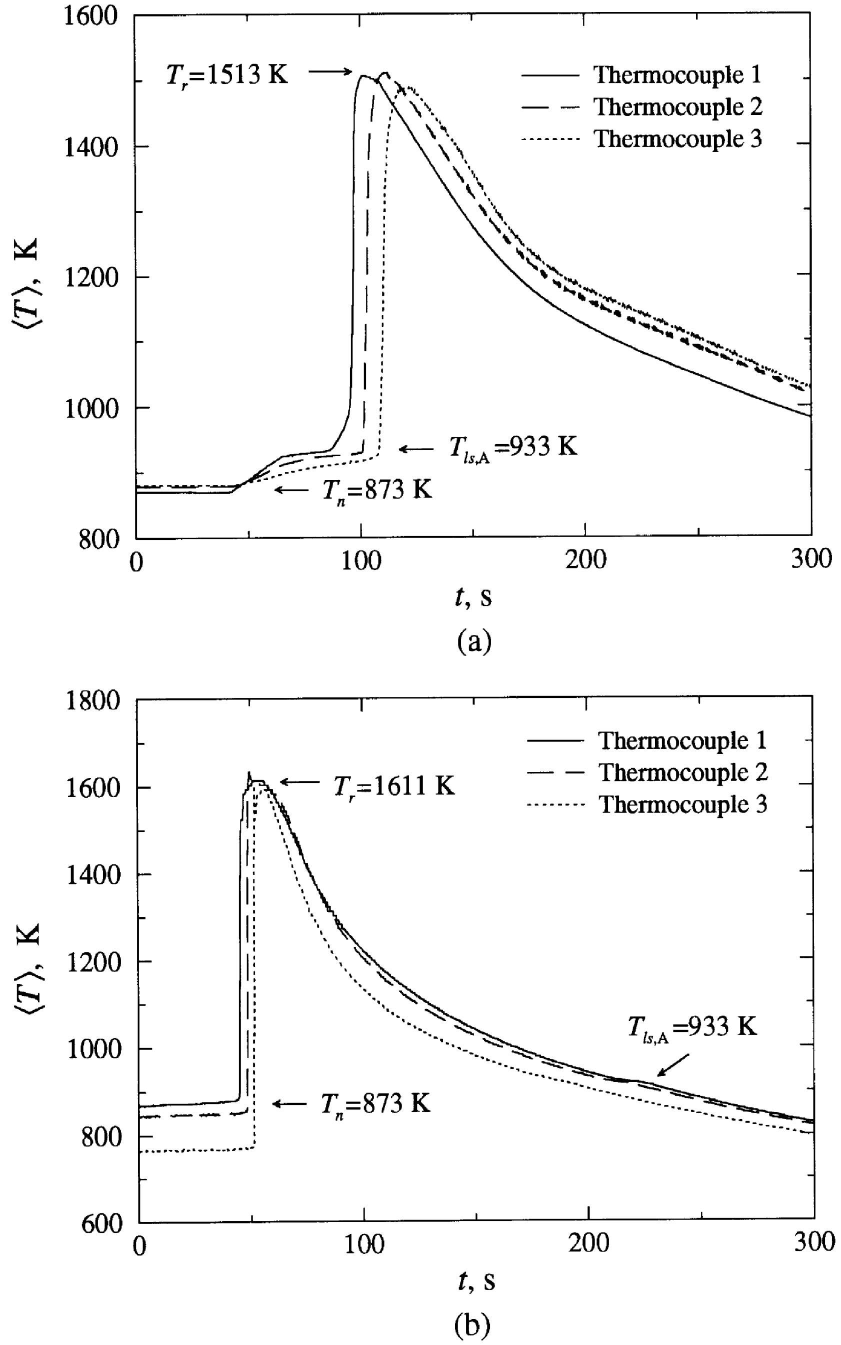

Fig. 4. Time variation of the measured temperature at three axial locations for (a) Test 3 and (b) Test 4.

After reaction, polished samples taken from a position between thermocouples 1 and 2, are observed on an electron microscope under BSEM (back-scattered scanning electron microscopy) mode and an XEDS (X-ray energy dispersive spectroscopy) analysis is performed to determine the particle-level atomic distribution. The XEDS analysis determines the average relative atomic compositions in a volume corresponding to a cube with sides of 5 μm. Figure 3(c) shows a typical BSEM micrograph of a polished section of the specimen. In this micrograph the largest particle is incompletely converted to $TiAl_3$. For this particle, the brighter central region is composed

Table 1
Maximum temperature and combustion front speed for the experiments

Test	$\overline{R_{B,n}}$ (μm)	T_1 (K)	T_2 (K)	T_3 (K)	$u_{F,v}$ (cm s^{-1})	$u_{F,1-2}$ (cm s^{-1})	$u_{F,2-3}$ (cm s^{-1})
1†	8.5	1529	1538	1513	0.27	0.32	0.27
2†	8.5	1523	1505	1481	0.22	0.34	0.26
3†	8.5	1506	1510	1488	0.22	0.32	0.23
4†	1.2	1613	1614	1607	0.80	0.81	1.02
5‡	1.2	1616	1637	1593	0.70	0.62	0.67
6‡	1.2	1663	1640	1516	0.70	0.65	0.64

† From CERAC Inc.
‡ From Alfa AESAR (Johnson–Matthey).

of Ti, the intermediate region is Ti_3Al, the external gray region is $TiAl_3$, and remaining aluminium is found at the surface. The gradient of concentration of aluminium along the Ti_3Al and $TiAl_3$ layers is below the spatial resolution of the XEDS analysis (it is estimated to be smaller than 5% by weight). The smaller particles are completely converted to $TiAl_3$. Image analysis of low magnification BSEM micrographs for the 325 MESH powders (using NIH Image) shows that the fraction of non-converted titanium cores corresponds to 1% of the total solid fraction, which corresponds to a conversion fraction $F_c = 0.96$. For the 1–3 μm powders only a few titanium cores (less than 0.1%) remain non-reacted ($F_c \simeq 1$). The total amount of intermediate compounds (e.g. Ti_3Al) was not measured.

3. Thermodynamic and thermophysical properties

The properties for Al, Ti and $TiAl_3$ are given in Table 2. The thermodynamic properties are determined in accordance with the assumptions used in the model developed in Part I. The specific heat capacity of $TiAl_3$ is obtained from Newman and Kopp's rule [10]. For the heat of formation of $TiAl_3$, Kubaschewski and Evans [7], Kubaschewski and Alcock [8], and Hultgren et al. [9], have reported -1.13×10^6 J $kg_{TiAl_3}^{-1}$ (we note that the more recent edition of Kubaschewski et al. [10] does not report any data for the Ti–Al system). Recently Zou et al. [11] have obtained a similar value for the heat of formation from 'ab-initio' computations for the Ti–Al system. To model the phase equilibrium at a particle level, a fifth-degree polynomial is curve fitted to the liquidus line for that section of the phase diagram between Al and $TiAl_3$.

Table 2
Thermophysical and thermochemical properties for the Al–Ti system

		Al	Ti	$TiAl_3$
M	kg kmol^{-1}	26.982	47.90	128.846
ρ	kg m^{-3}	2700	4500	3310
c_p	J kg^{-1} K^{-1}	1090	654	928
k	W m^{-1} K^{-1}	225	20	50
T_{ls}	K	933	1943	1647
T_b	K	2793	3562	
Δi_{ls}	J kg^{-1}	3.97×10^5	3.05×10^5	1.38×10^6
i_f^o	J kg^{-1}	0	0	-1.13×10^6

The transport properties are modeled in a semi-empirical way. The effective thermal conductivity $\langle k \rangle$ is obtained from a model developed by Hadley [12]. It is assumed that both the non-reacted material ($\langle T \rangle < T_{ls,A}$) and the reacted material ($\langle T \rangle > T_{ls,A}$) have constant, but different, effective thermal conductivities. The effective peripheral heat transfer coefficient h_{sa} is obtained from the cooling (i.e., post-reaction) region of the measured temperature distribution, with the assumption that no residual chemical reaction occurs during the temperature decay. Note that h_{sa} contains contributions from radiation (which is the prevailing heat transfer mode between the specimen and the heater) and convection (which has a heating effect in the reacted region, instead of a cooling effect, because the propagation is downwards and an opposing argon flow is maintained during the test). The diffusion coefficient of aluminium in the diffusion layer is estimated from values available in the literature and from the measurements. Sprengel et al. [13] report experimental results for the diffusion coefficients of Al and Ti, in nearly stoichiometric TiAl (TiAl crystallizes in the $L1_0$ structure while $TiAl_3$ crystallizes in the $D0_{22}$ structure). For the inter-diffusion coefficient, their own measurements (using diffusion couples) provided $D_o = 2.8 \times 10^{-4}$ m^2 s^{-1} and $\Delta E_{a,D} = 2.95 \times 10^8$ J kmol^{-1} for the temperature range of 1116 to 1583 K. They also determined the self-diffusion coefficients of Al and Ti (using radioactive tracers and Darken's model) and found no difference between the inter-diffusion and the self-diffusion coefficients, within the experimental uncertainty. To the authors knowledge, there are no available diffusion data for the diffusion of Al and Ti in $TiAl_3$. In the absence of data, Machlin [14] recommends to calculate the activation energy for the diffusion coefficient of alloys as 18 $R_g\ T_{ls,C}$ where R_g is the universal gas constant and $T_{ls,C}$ is the solidus line temperature for the alloy. For $TiAl_3$, this gives 2.5×10^8 J kmol^{-1}. Hanamura [4], performing combustion synthesis experiments with $TiAl_3$ at different T_n has obtained values of the order of 2×10^8 J kmol^{-1} from Arrhenius plots [23]. Based on these estimates, the value of 2×10^8 J kmol^{-1} is used in the computations. The pre-exponential factor for the diffusion coefficient, in absence of any specific data, is chosen to match the predicted and measured results of the propagation speed ($u_F = 0.25$ cm s^{-1}). As it will be shown later, the value obtained is $D_o = 4.39\times 10^{-4}$ m^2 s^{-1}.

4. Numerical integration of governing equations

The conservation equations presented in Part I [1] are solved numerically using the finite-volume method. The solution scheme includes nonuniform grid, implicit discretization of the transient term, staggered grid for the velocity, the power-law scheme for the treatment of the diffusion–convection fluxes, and the TDMA algorithm for solving the algebraic equations. The equations are solved in their transient form as an aid to achieve convergence. The domain used (in the transformed variable $x_1 = x+u_F t$ where u_F is the speed of the combustion front) is equivalent to 0.3 m. This domain is large enough to assure negligible boundary effects (the flame thickness being of the order of 1 cm). The grid is divided into a uniform grid in the reaction region and nonuniform grids in the preheat and reacted regions. To test the grid dependency of the results, a grid with 151 nodal points, $\Delta x_1 = 0.26$ mm in the reaction region, and one with 301 nodal points, $\Delta x_1 = 0.104$ mm in the reaction region were used. The increase in the number of grid nodes did not make an appreciable change in the flame speed and the maximum temperature. For the adiabatic system and stoichiometric conditions, the solution with 151 nodal points predicted a maximum temperature of 1647 K and a fraction of liquid product of 0.299, against a thermodynamic determined adiabatic temperature of 1647 K and a fraction of liquid product of 0.307. As a result, the grid with 151 nodal points was adopted. A small Δt (i.e., $\Delta t = 10^{-4}$ s) was necessary for stable convergence.

The iterations begin by a guessed specimen-level temperature and species A concentration distributions (usually, those from a previous run). From the concentration of species A, the other species concentrations are computed. Then from the particle-level equations, the various radii in the unit cell, and the volume-averaged density of the diffusion layer are computed, followed by the computation of the reaction and melting rates. Special attention is required for the detection and treatment of the various transitions (transition from the primary- to secondary-diffusion regime, melting of species A, and solidification of species C). From the reaction rates, the propagation speed is determined. Then the specimen-level conservation equations are solved for $\langle \rho_A \rangle$ and $\langle T \rangle$, starting the next iteration. Convergence is assumed when the steady-state overall energy balance (the sum of the convective and diffusive fluxes and the heat generated relative to the heat generated) is smaller than 0.1%. At this point, the combustion-front speed and the maximum temperature vary by less than 0.1%.

During the iterations, when the front speed u_F has not yet reached its steady-state value, the combustion front tends to move away from the refined portion of the grid. To hold the flame, a moving grid technique is used. After moving a short distance from the center of the grid, all the variables are moved back, using a linear interpolation to compute the new values at the nodal points. After reaching a certain convergence, the grid movement is turned off and the specimen-level variables and the flame speed are allowed to converge.

5. Results and discussion

5.1. Effect of particle-size distribution on conversion to final product and maximum temperature

The particle-size distribution influences the intraparticle and interparticle diffusion, as discussed in Oliveira and Kaviany [1]. First, the effect in the interparticle diffusion is analyzed.

Using the Weibull distribution, equation (1), in the interparticle diffusion model described in Part I, the fraction of component A (i.e., aluminium) converted to the final products F_c is determined using equation (I.40) (I.40 refers to equation (40) in Part I). For $R_o = 0$ we obtain,

$$F_c = e^{-\left(\frac{\overline{R_{B,n}}}{\theta}\right)^b} + \left(\frac{\theta}{\overline{R_{B,n}}}\right)^3 \int_0^{\left(\frac{\overline{R_{B,n}}}{\theta}\right)} \eta^{3/b}\, e^{-\eta} d\eta, \tag{2}$$

where $\overline{R_{B,n}}$ is given by

$$\left(\frac{\overline{R_{B,n}}}{\theta}\right)^3 = \int_0^{\infty} \eta^{3/b}\, e^{-\eta}\, d\eta. \tag{3}$$

Figure 5(a) shows the behavior of the Weibull distribution for $R_o = 0$, and several different values of b. For $R_o = 0$, F_c is a function of b only and is shown in Fig. 5(b). As b increases, the standard deviation of the distribution function decreases and the extent of conversion to the final products increases. For small values of b, the standard deviation and the skewness towards small values of R_B increase, causing a decrease in the conversion fraction. In the absence of interparticle diffusion, the maximum temperature that can be possibly achieved in the combustion region T_{max} can be calculated once the particle-level reactions are known. For the

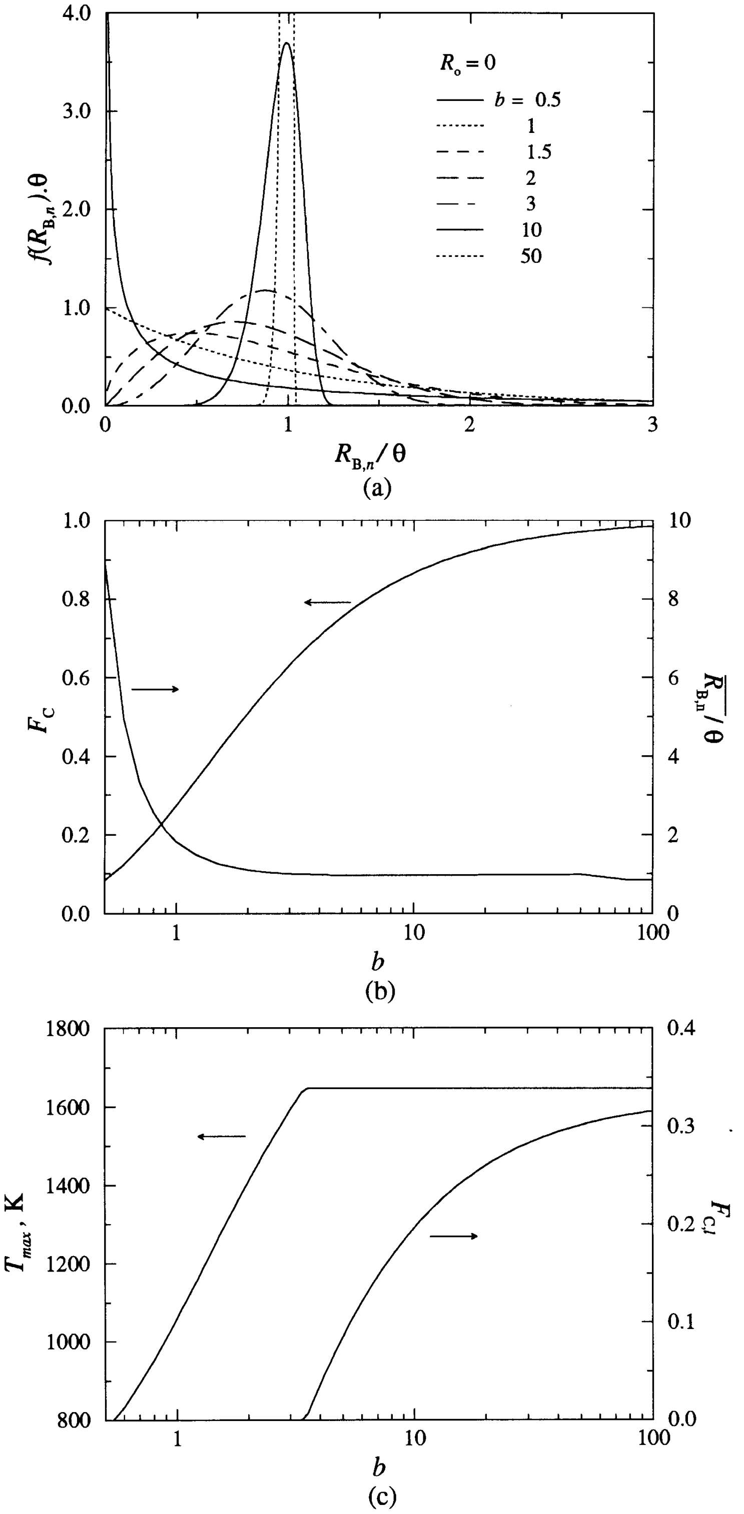

Fig. 5. (a) Weibull distribution function for $R_o = 0$ and several different values of the shape parameter b and variations with respect to b of the (b) conversion fraction F_c and average particle radius $\overline{R_{B,n}}$, and (c) maximum temperature T_{max} and fraction of liquid product $F_{C,l}$.

titanium–aluminium system, $TiAl_3$ is the first compound to form at the interface between aluminium and titanium [16]. Assuming constant specific heats $c_{p,l} = c_{p,s}$, $\Delta c_p = 0$, and ideal solution (see Part I for a discussion on thermodynamics) the maximum temperature possible in the combustion front is determined from

$$T_{\max} = T_n + \frac{Y_{A\text{–}C}}{c_{p,C}}\left(-\Delta i_{ls,A} - F_c\left(\frac{i^{o}_{f,C}}{Y_{A\text{–}C}} - \Delta i_{ls,A}\right)\right). \quad (4)$$

Figure 5(c) shows $T_{\max}$ as a function of the shape parameter b. Similarly to F_c, $T_{\max}$ increases with an increase in b, reaching the adiabatic equilibrium temperature T_{ad} for sufficiently large values of b. The fraction of liquid product $F_{C,l}$ when $T_{\max} > T_{ls,C}$ is determined from

$$F_{C,l} = \frac{c_{p,C}(T_{\max} - T_{ls,C})}{-i^{o}_{f,C} - Y_{A\text{–}C}\Delta i_{ls,A}} \quad (5)$$

and the results are also shown in Fig. 5(c).

The product liquid fraction $F_{C,l}$ begins to increase when the maximum temperature reaches the melting temperature of species C and reaches the thermodynamic equilibrium value of 0.307 for large values of b.

From Fig. 5(b), for the value of $b = 1.7$ determined for the 325 MESH Ti particles, we obtain $F_c = 0.456$ and $T_{\max} = 1328$ K. For the 1–3 μm Ti particles, from $b = 2.7$, we obtain $F_c = 0.602$ and $T_{\max} = 1545$ K. In both cases, the maximum temperatures are smaller than the measured reaction temperatures, whose averages are $T_r = 1510$ K and $T_r = 1611$ K (Table 1). For the 325 MESH Ti particles, the measured conversion fraction $F_c = 0.96$ corresponds to $b = 36$ which gives $T_{\max} = 1647$ K and $F_{C,l} = 0.29$. Compared to the reaction temperature, there is an excess energy of $c_{p,C}(T_{\max} - T_{ls,C}) + F_{C,l}\Delta i_{ls,C} = 5.27 \times 10^5$ J kg_C^{-1} which must be lost to the ambient as heat losses. Possible sources of error in the analysis are related to the thermodynamic properties and the interparticle-diffusion model. The specific heat capacity for the product may be underestimated and the heat of formation may be overestimated. In the interparticle-diffusion model, there are the difficulties in characterizing the shape of the particles and measuring the particle-size distribution. However, most importantly, the model developed here neglects the movement of the liquid species A from the A-rich regions to the A-lean regions. This movement is responsible for the complete conversion under adiabatic, equilibrium conditions. Some movement of A-liquid during the time scale of the reaction could cause an additional conversion and a temperature rise. The model used is an approximation for the limit of a high peripheral heat loss or a large tortuosity of the connected pores (large resistance to the interparticle diffusion). The intraparticle diffusion, specially the secondary-diffusion regime, enhances the effect of the heat losses, because it extends the reaction and the melting of products over a larger region of the specimen. For slow liquid migration conditions, the interparticle diffusion would become the rate-controlling mechanism, extending the reaction zone and allowing for a larger effect of the heat losses. That could allow for a lower reaction temperature along with a larger conversion as observed in the experiments. The effects of the intraparticle diffusion and melting of product is discussed in the next sections.

5.2. Effect of intraparticle diffusion on combustion front structure and microstructure

The results for the 325 MESH titanium particles are used to study the effect of the intraparticle diffusion. In order to study the effects of the intraparticle-diffusion independently from the effects of the interparticle-diffusion, a value of $b = 2.7$ is adopted, giving $T_{\max} = 1546$ K which is closer to the experimental value of the maximum temperature. The Weibull distribution functions for $b = 1.7$ and $b = 2.7$ are compared with the measured particle-size distribution values in Fig. 1(b). From $b = 2.7$ and $\theta = 8.4$ μm an average radius of 8.5 μm is calculated using equation (I.33). From this value, the conversion fraction is $F_c = F_{A,c} = F_{B,c} = 0.602$. This corresponds to 60% conversion to $TiAl_3$. From this unit-cell average stoichiometry, the values in the second column of Table 3 (average-particle model) are calculated and used in the computations.

Figure 6 shows the comparison between the predicted and measured temperature distributions for Test 3. The variation of the measured temperature distribution with respect to time is converted to that with respect to the moving coordinate $x_1 = x + u_F t$ using $u_f = 0.25$ cm s^{-1}. In comparing Fig. 6 to Fig. 4, note that, for a closer examination, only part of the measured temperature distribution is used (the computational domain corresponds to ± 60 s around the combustion front). The ignition temperature is assumed as being $T_{ls,A}$, which is equivalent to assume that $\langle \dot{n}_{r,A} \rangle$ is zero for $\langle T \rangle < T_{ls,A}$. The localized melting of species A at $T_{ls,A}$ causes a sharp change in slope in the distribution of $\langle T \rangle$. Right after the melting of species A, reaction starts and the heat liberated raises the temperature to nearly the maximum temperature $T_{\max} = 1515$ K. The model predicts a thinner reaction region compared to that measured. The predicted temperature distribution is plotted such that the transition from the primary to the secondary-diffusion regime occurs at $x_1 = 0.15$ m. At the end of the primary-diffusion regime the predicted temperature is 1323 K. During the secondary-diffusion regime there is an additional heating of 192 K before the reaction rate decreases. The measured temperature distribution shows a transition at $T = 1370$ K, from a steep temperature rise to a smaller slope. The inability of the model to predict the temperature distribution closely, shows the importance of the inter-

Table 3
Effective properties for the Al–Ti specimens at the 3:1 composition

		Average-particle model	Distributed-particle model (8-bins)
ε_n		0.30	0.30
$\overline{R}_{B,n}$	m	8.5×10^{-6}	8.62×10^{-6}
$\overline{R}_{A,l,n}$	m	11.8×10^{-6}	13.95×10^{-6}
l	m	24.12×10^{-6}	24.46×10^{-6}
$\langle k\rangle_n$, $\langle k\rangle_r$	$W\,m^{-1}K^{-1}$	7,30	7,30
$\langle k_r\rangle$	$W\,m^{-1}\,K^{-1}$	0.0015	0.0015
h_{sa}	$W\,m^{-2}\,K^{-1}$	45	45
D_o	$m^2\,s^{-1}$	2.54×10^{-4}	4.39×10^{-4}
ΔE_d	$J\,kmol^{-1}$	2.0×10^8	2.0×10^8
Stoichiometric condition			
$Y_{A\text{-}C}$		0.628	0.628
$\langle\rho\rangle$	$kg\,m^{-3}$	2220.15	2220.15
$\langle\rho_A\rangle_n$	$kg\,m^{-3}$	1394.78	1394.78
$\langle\rho_B\rangle_n$	$kg\,m^{-3}$	825.37	825.37
A-lean condition			
F_c		0.602	0.581
$\langle\rho\rangle$	$kg\,m^{-3}$	1665.03	1635.74
$\langle\rho_A\rangle_n$	$kg\,m^{-3}$	839.66	810.37
$\langle\rho_B\rangle_n$	$kg\,m^{-3}$	825.37	825.37
$\langle\rho_A\rangle_{tran}$	$kg\,m^{-3}$	610.45	610.45

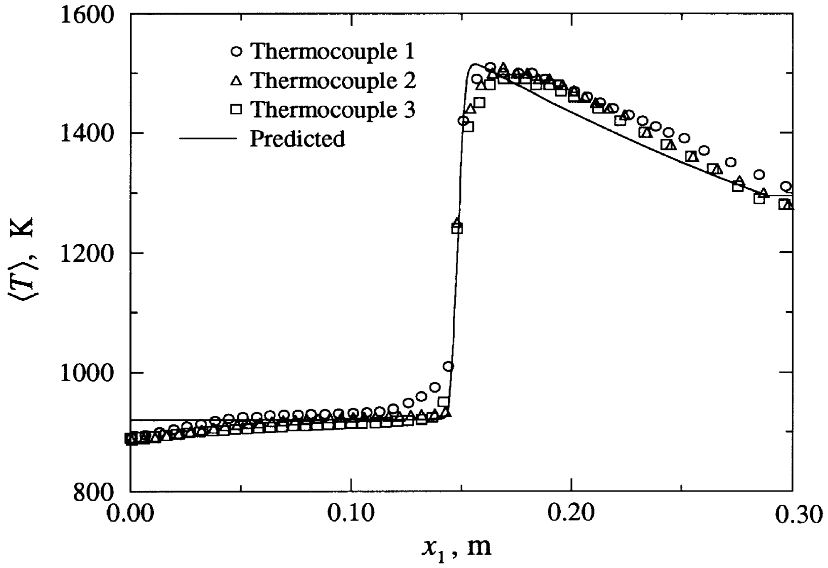

Fig. 6. Measured and predicted temperature distributions along the moving axis x_1. The experimental results are for the three thermocouples in Test 3.

particle diffusion. The liquid migration from the melt-rich to the melt-lean regions may be modeled as a diffusion process which occurs in series with the intra-particle diffusion. This would reduce the reaction rate during the secondary-diffusion regime. The detailed account of the effect of the particle-size distribution on the reaction rate will be discussed later. First other aspects of the model are analyzed.

Figure 7 presents the predicted distribution of the specimen-level variables. Figure 7(a) presents the distribution of temperature and species A and C concentrations along the specimen. The distribution of species A includes the fraction of non-reacted material and is normalized with respect to the stoichiometric non-reacted concentration of species A (Table 3). Similarly, the species C concentration is normalized with respect to the stoichiometric reacted concentration of species C (Table 3). The volume-averaged temperature $\langle T\rangle$ is normalized with respect to $T_{\mathrm{ad}} = 1647$ K. The maximum value for $\langle T\rangle$ reached in the combustion region is $T_{\mathrm{r}} = 1515$ K and the maximum value for $\langle T\rangle$ possible is $T_{\max} = 1545$ K. Therefore, heat loss causes a reduction in T_{r} of only 30 K. Figure 7(b) shows the distribution of the reaction rate. The reaction rate distribution starts with a spike which is caused by the infinite reaction rate calculated form the primary-diffusion regime equations when the product layer thickness is zero. This is dealt with here through the creation of a fictitious initial product layer with a thickness of $0.001R_{\mathrm{B,n}}$ covering the species B particles. This initial product layer plays a role similar to that of a surface kinetic-controlled reaction, which could be caused by the presence of an oxide layer or due to the nucleation kinetics of the product phase. The transition from the primary- to secondary-diffusion regime is characterized by a jump in the reaction rate, due to the approximations used in the solution of the mass diffusion problem (the first-order integral solution for the secondary-diffusion regime). Figure 7(c) shows the rate of product phase change. The positive values of $\langle\dot{n}_{\mathrm{ls,C}}\rangle$ are associated with the melting of C and the negative values are associated with the solidification of C. Melting takes place continuously along the reaction region and solidification occurs instantly when the mass fraction of species A at R_{C} becomes smaller than the mass fraction of species A in the liquidus line (Fig. 8(c)). Figure 7(d) shows a rather insignificant formation of liquid

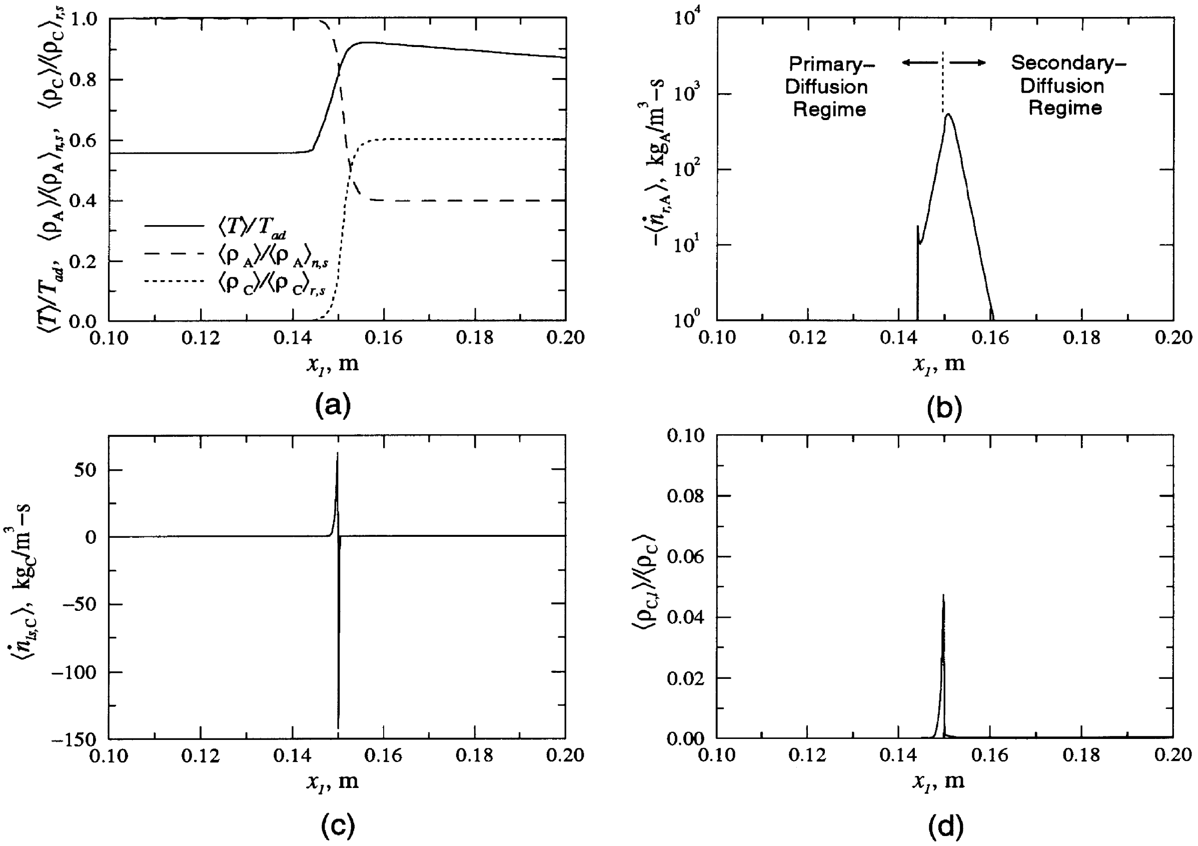

Fig. 7. Predicted, axial (moving coordinate) distribution of the specimen-level variables. (a) Local volume-averaged temperature and species A and C concentration distributions, (b) species A reaction rate, (c) product C melting rate, and (d) product liquid fraction. The predicted front speed is $u_{\mathrm{F}} = 0.25$ cm s^{-1}, the adiabatic temperature is $T_{\mathrm{ad}} = 1647$ K, the nonreacted stoichiometric concentration of species A is $\langle\rho_{\mathrm{A}}\rangle_{\mathrm{n,s}} = 1394$ kg m^{-3}, and the reacted stoichiometric concentration of species C is $\langle\rho_{\mathrm{C}}\rangle_{\mathrm{r,s}} = 2220$ kg m^{-3}.

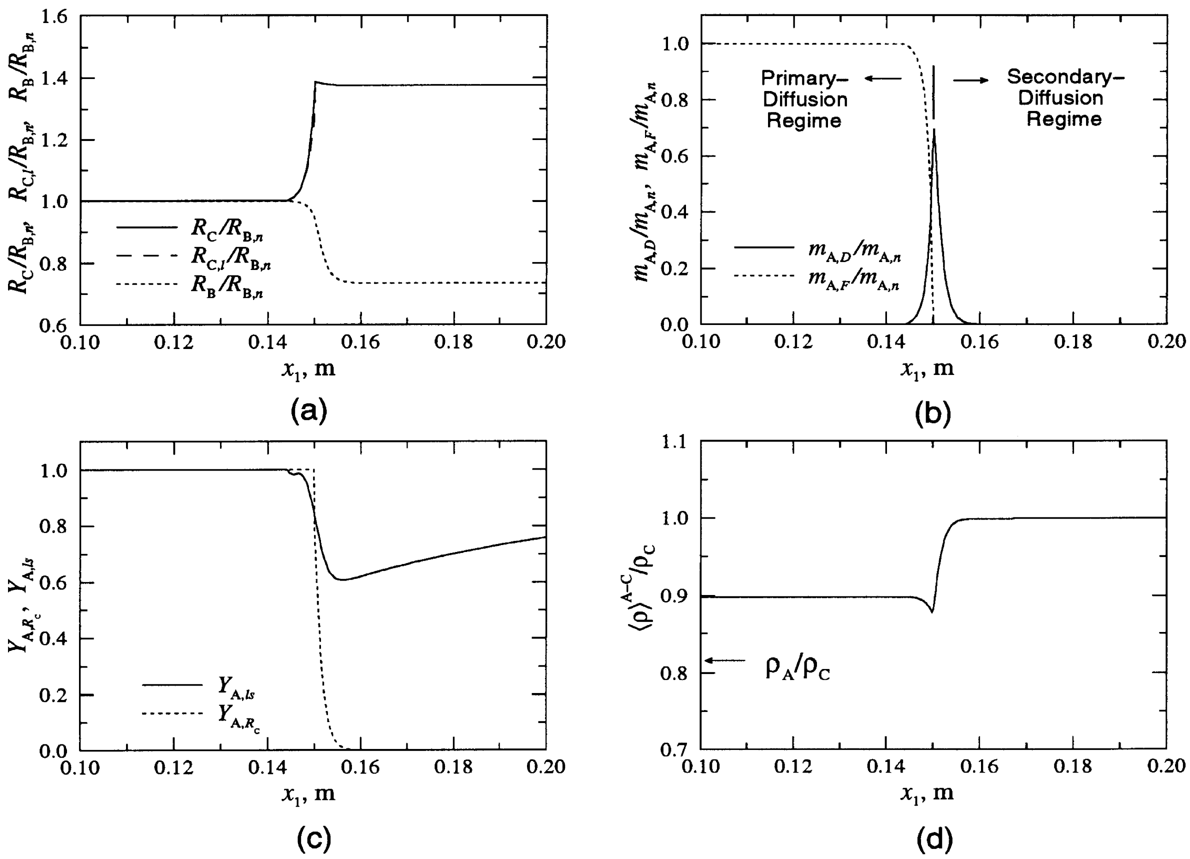

Fig. 8. Predicted, axial (moving coordinate) distribution of the particle level variables. (a) Species B particle radius R_B, product C spherical shell radius R_C, and liquid product C,l spherical shell radius, (b) mass of species A diffused into the diffusion layer $m_{A,D}/m_{A,n}$ and that available outside the diffusion layer $m_{A,F}/m_{A,n}$, (c) the mass fraction of species A at R_C and the liquidus-line mass fraction of species A and (d) the normalized local volume-averaged density of the diffusion layer.

product. This occurs because, for the Al–Ti system, the liquidus line near the pure aluminium side of the phase diagram is steep (Fig. I.2(c)).

Figure 8 presents various aspects of the particle-level structure. Figure 8(a) presents the evolution or R_B, $R_{C,l}$ and R_C along the specimen, normalized with respect to the average initial radius of species B, $\overline{R_{B,n}}$. Figure 8(b) presents the variations of the mass of aluminium diffused into the diffusion layer $m_{A,D}$ and the mass of aluminium available outside the diffusion layer $m_{A,F}$ referenced to the initial mass of aluminium ($m_{A,n} = \langle\rho_A\rangle_n l^3$), as a function of x_1. The transition from the primary-diffusion regime to the secondary-diffusion regime takes place where $m_{A,F} = 0$. Figure 8(c) presents the evolution of the mass fraction of species A at R_C, Y_{A,R_C}, and the mass fraction of species A at the liquidus line, $Y_{A,ls}$, along the specimen. The mass fraction of species A at R_C, Y_{A,R_C}, is equal to 1 for the primary-diffusion regime. It decreases for the secondary-diffusion regime and reaches 0 when all the available mass of species A (taking into account the conversion fraction) is converted. As the temperature varies along the specimen, the value of $Y_{A,ls}$ varies accordingly. It reaches a minimum for $\langle T\rangle_r$ and increases again as $\langle T\rangle$ decreases. The product solidification takes place where $Y_{A,R_C} = Y_{A,ls}$. Figure 8(d) shows the variation of the density of the diffusion layer, $\langle\rho\rangle^{A\text{–}C}$, normalized with respect to the product density ($\rho_C = 3310$ kg m^{-3}) along the specimen. During the primary-diffusion regime, there is an aluminium enrichment of the diffusion layer and during the secondary-diffusion regime there is an aluminium consumption. This density variation across a layer of solid products causes the development of internal stresses which can cause the cracking of the particles.

The model is now compared with simpler models and the role of the secondary-diffusion regime is explored.

5.2.1. *Role of secondary-diffusion regime*

In the secondary-diffusion regime the reaction rate is lower than that in the primary-diffusion regime. This tends to enlarge the reaction region. The two-regime model is compared with a model that includes only the primary-diffusion regime, i.e., a single-regime model, and to a homogenous premixed-type model. For simplicity, species A is assumed to react in the solid phase (this is equivalent to discarding the localized melting of species A and allowing for it by subtracting the heat of melting of species A from the heat of reaction)(e.g., Kaper et al. [17]).

In the single-regime model, the reaction rate is determined for the primary diffusion regime (quasi-steady approximation) for the entire specimen-level domain [18,19,21]. This reaction rate diminishes monotonically with decreasing R_B. The various radii and the density of the diffusion layer are determined in the same manner as described above. For the premixed-type model, the simplest available kinetic model, a homogeneous first-order kinetics, is assumed. The local volume averaged reaction rate is given by

$$\langle \dot{n}_{r,A} \rangle = A_o \langle \rho_A \rangle \exp\left(\frac{-\Delta E_a}{R_g \langle T \rangle}\right), \qquad (6)$$

where A_o is the effective pre-exponential factor (constant).

Figure 9(a) presents the measured temperature distribution for Test 3 and the local volume-averaged temperature distributions predicted by the two-regime, the single-regime, and the premixed-type models. All the parameters in Table 3 have been kept constant for the three models, except the pre-exponential factor. The pre-exponential factor for the single-regime and the premixed-type models are chosen to match the predicted and measured propagation speed ($u_F = 0.25$ cm s^{-1}). Note that none of the three models are able to predict accurately the behavior near the maximum temperature and the single-regime and the premixed-type models behave approximately in the same way. Figure 9(b) presents the distribution of the volume-averaged reaction rate predicted by the three models. The secondary-diffusion regime has a small effect on extending the reaction zone. This occurs because, for the conversion fraction used, the species A available is rapidly consumed during the primary-diffusion regime and the beginning of the secondary-diffusion regime. Once the reaction rates decrease by one order of magnitude the temperature distribution becomes controlled by the balance between storage and heat loss. The first-order premixed model is able to predict the combustion front structure with reasonable accuracy. This characterizes a thin combustion front and the propagation speed could be estimated using, for example, the models developed by Armstrong [19] and Kaper et al. [17].

Comparing with the premixed-type kinetics, the expressions for the reaction rates for the primary- and secondary-diffusion regimes in the two-regime model, can be rewritten as

$$\langle \dot{n}_{r,A} \rangle_1 = -\langle \rho \rangle A_{o,1} \; D_{A\text{–}C} \qquad (7)$$

$$\langle \dot{n}_{r,A} \rangle_2 = -\langle \rho \rangle A_{o,2} \langle Y_A \rangle \; D_{A\text{–}C} \qquad (8)$$

where $A_{0,1}$ and $A_{0,2}$ are effective pre-exponential factors.

Figure 10 shows the variation of these effective pre-exponential factors as a function of $Y_A = \langle \rho_A \rangle / \langle \rho \rangle$, where $\langle \rho \rangle$ is the total density and $\langle \rho_A \rangle$ is the concentration of species A (excluding the non-reacted mass of species A). The continuous line identifies the transition from the primary- to the secondary-diffusion regimes. We observe a variation of about five orders of magnitude in A_o between the primary-diffusion regime and the secondary-diffusion regime. The effective pre-exponential factors depend on the stoichiometry, initial particle size, and $\langle \rho_A \rangle$. The premixed-type model follows the behavior of the secondary-diffusion regime but not of the primary-diffusion regime [Fig. 9(a)]. Although not shown in Fig. 10, the heterogeneous kinetics models used by Aldushin et al. [22] and Dunmead and Munir [23] were compared to the two-regime model predictions and they also do not follow the behavior of the primary-diffusion regime.

5.2.2. *Role of product phase change*

The phase change of species C depends on the features of the phase diagram for the binary system. For the Al–Ti system, the liquidus line near the pure aluminium side is almost vertical, causing a negligible melting of product C in the temperature range observed in the experiments. However, other intermetallic systems with different phase diagrams can have a more pronounced product melting. In order to analyze the effect of phase change on the front structure, propagation speed, and maximum temperature, the liquidus line will be modeled as a straight line with slope given by

$$\gamma = \frac{dT_{ls}}{dY_{[A],ls}}. \qquad (9)$$

For T_{max} as the maximum temperature possible in the reaction region, γ can be modeled as

$$\gamma = \frac{T_{ls,A} - T_{max}}{1 - Y_{[A],ls}(T_{max})}. \qquad (10)$$

For intermetallic systems with a constant slope for the liquidus near the low-melting temperature metal (as in the Al–Ni or in the Al–Co systems), γ can be modeled as

$$\gamma = \frac{T_{ls,A} - T_{ls,C}}{1 - Y_{[A]\text{–}C}}. \qquad (11)$$

Table 4 presents characteristic values of γ for some metallic systems. The two-regime model is solved for three values of γ, i.e., -7860, -1920, and -1500 K. The first value is representative of the Al–Ti system, the second value is representative of the Al–Ni system, and the third is representative of the Al–Fe system. The other thermophysical properties are kept constant (Table 3). Table 5 lists the predicted results and Fig. 11(a) presents the local volume-averaged temperature and species A distributions. The larger the value of γ the larger is the

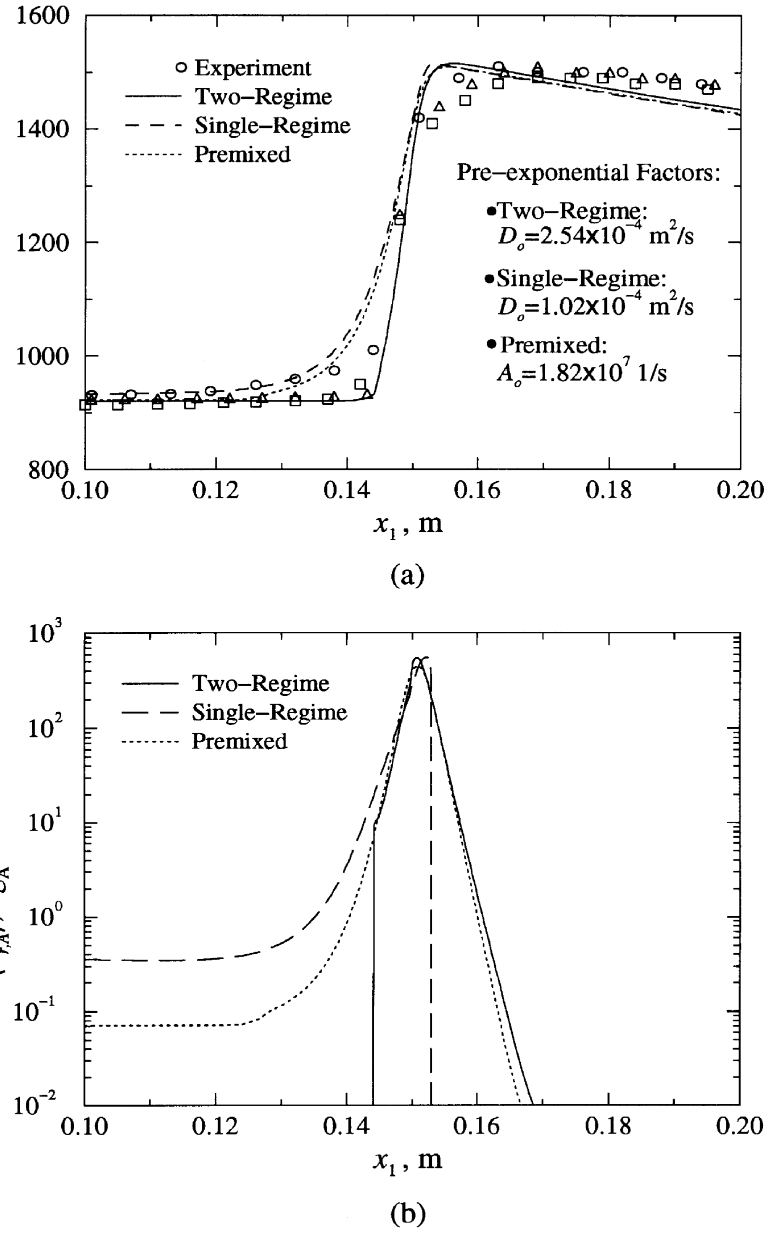

Fig. 9. (a) Measured and predicted temperature distributions along the moving axis x_1 (the experimental results are for the three thermocouples in Test 3) and (b) reaction rate distributions predicted by the two-regime, single-regime and premixed-type models.

production of liquid. As γ increases, there is initially an increase in the maximum temperature. This is due to the energy released from the solidification of the product near the maximum temperature (Fig. 11(c)). This local generation of energy causes a smaller heat loss compared to the distributed generation. A further increase in γ results in a decrease in the maximum temperature, because the product melting delays the temperature evolution, thus increasing the thickness of the reaction region δ_F and the effect of the heat loss. The smaller rate of increase of the temperature as γ increases causes the propagation speed to decrease—(melting of product is known to be a destabilizing factor (e.g., Kaper et al. [17])). Figures 11(c) and (d) show the distribution of the product melting rate and the liquid product mass fraction. For large volumes of liquid, the specimen can lose its structural stability, as observed for the Al–Ni system.

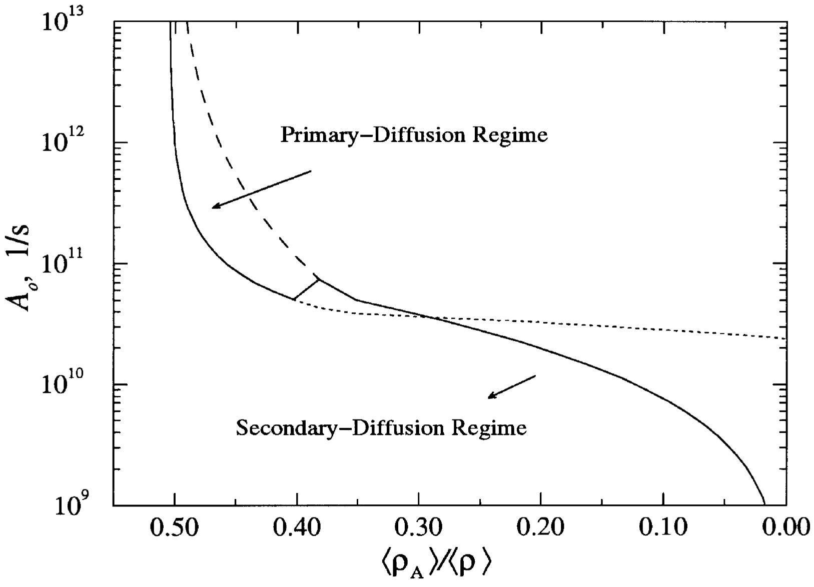

Fig. 10. The variation of the effective pre-exponential factors with respect to the mass fraction of species A, as predicted by the two-regime model.

Table 4
Slope of the liquidus line for some metallic systems

System	T_{max} or T_{ls} (K)	γ (K)
Al–Ti	$T_{r,Al_3Ti} = 1513$	-7860
Al–Ni	$T_{ls,Al_3Ni} = 1373$	-733
	$T_{ls,AlNi} = 1911$	-3056
Al–Fe	$T_{ls,Al_3Fe} = 1430$	-828
Al–Co	$T_{ls,AlCo} = 1921$	-3293
Al–Cr	$T_{ls,Al_4Cr} = 1453$	-764
	$T_{ls,AlCr} = 2136$	-1203

Table 5
Predicted results for the effect of phase-equilibrium

γ (K)	u_F (cm s^{-1})	T_r (K)	δ_F (cm)
-7860	0.250	1515	1.66
-1920	0.197	1506	1.95
-1500	0.116	1463	2.05

5.3. *Effect of particle-size distribution on reaction rate*

The particle-size distribution function has been approximated by a discrete distribution with eight bins. The height of the bins was chosen to conserve the area under the curve (for the corresponding species B particle size range). Each probability is associated with the particle radius at the center of each bin. For each bin, the subunit-cell parameters are calculated following the discussion in Part I. Table 6 presents the size, probability, and initial (non-reacted) concentrations for the subunit cells. In Table 6, the concentration of A decreases with an increase in the radius of the species B particles because the mass of species A is constant while the characteristic length of the subunit cells l_i increases to keep the porosity ε_n constant. The value of $\langle\rho_A\rangle$ at the transition from the primary-diffusion regime to the secondary-diffusion regime $\langle\rho_A\rangle_{tran}$, decreases with an increase in the size of the species B particles because the volume of the diffusion layer increases. The particles with $R_{B,n} \leqslant 1.5\ \mu$m are completely converted during the primary-diffusion regime.

Figure 12(a) presents the local volume-averaged temperature and species A concentration distributions calculated using the average-particle model and the distributed-particle model (8 bins). In order to predict the experimental result for the propagation speed (0.25 cm s^{-1}), the distributed-particle model requires setting $D_o = 4.39 \times 10^{-4}$ m^2 s^{-1}, which is 70% larger than the pre-exponential factor used for the average-particle model. This difference indicates that the average particle radius given by equation (I.33) does not represent the average behavior of the unit cell. Also shown are the local volume-averaged concentration distributions of species A determined for each subunit cell. The topmost curves correspond to the smaller species B particles (the size of the species B particles increases from top to bottom). The smaller species B particles occupy a smaller fraction of the subunit cell. In order to keep the porosity constant,

Table 6
Effective properties for subunit cells for the 8-bin distribution

Bin no.	$R_{B,i,n}$ (μm)	$f_i \times 10^{-6}$	$l^3 \times 10^{-18}$ m^3	$\langle\rho_A\rangle_n$ (kg m^{-3})	$\langle\rho_B\rangle_n$ (kg m^{-3})	$\langle\rho\rangle$ (kg m^{-3})	$\langle\rho_A\rangle_{tran}$ (kg m^{-3})
1	1.5	0.020052	22.11	1886.47	5.88	1892.35	—
2	4.5	0.090542	22.47	1799.11	151.48	1950.59	1627.42
3	7.5	0.122819	23.70	1531.75	597.08	2128.83	1218.35
4	10.5	0.075644	26.07	1151.20	1231.34	2382.54	830.43
5	13.5	0.021493	29.44	799.49	1817.51	2617.00	542.04
6	16.5	0.002652	33.52	541.49	2247.52	2789.01	353.91
7	19.5	0.000130	38.07	369.81	2533.65	2903.46	236.55
8	22.5	0.000002	42.90	258.38	2719.37	2977.75	163.14

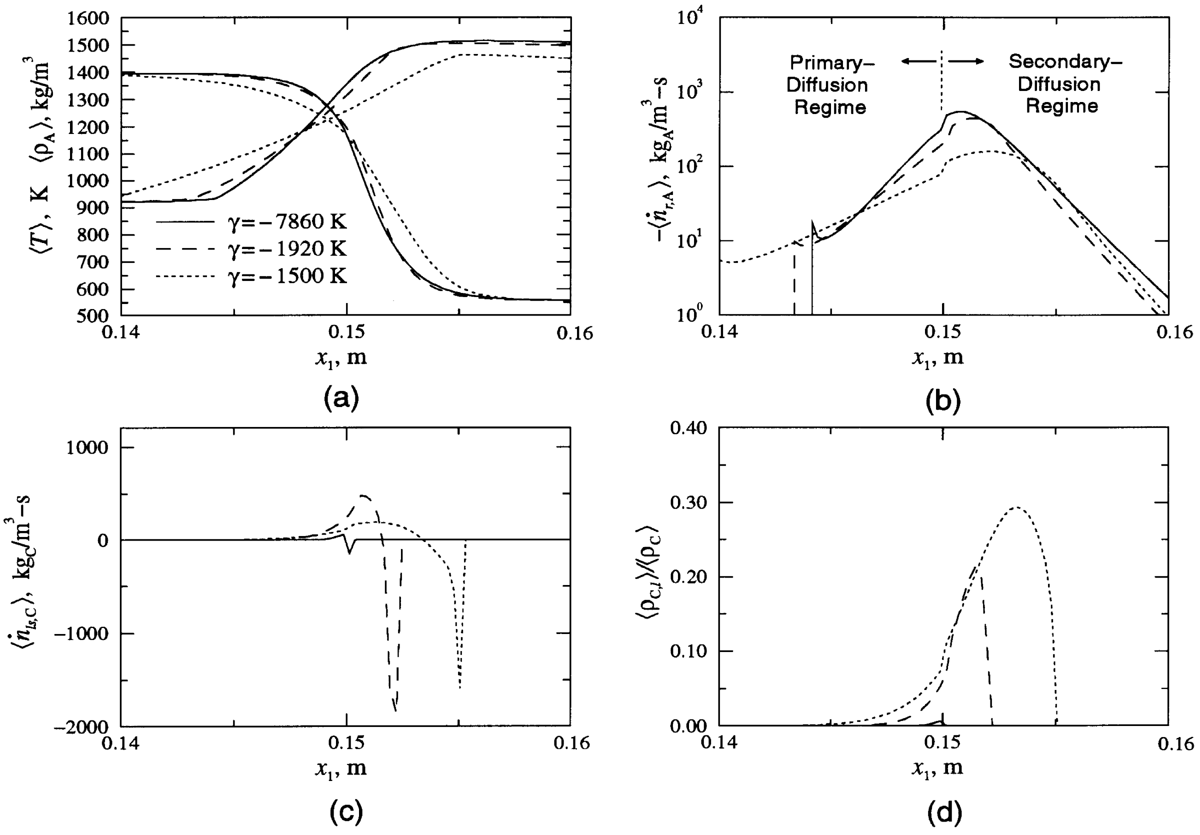

(a) (b) (c) (d)

Fig. 11. Effect of the product phase change. (a) Variation of the local volume-averaged temperature and species A concentration distributions, (b) product melting rate and (c) liquid product fraction, as predicted by the two-regime model for three values of the liquidus-line slope γ.

the dimension of the unit cell becomes smaller and species A occupies a larger fraction of the subunit cell. Additionally, a small amount of species A is enough to convert the small species B particles, thus resulting in a small variation of the species A concentration. On the other hand, for the larger species B particles, all the species A available in the subunit cell is converted. The maximum temperature predicted by the distributed-particle model is 27 K lower than the predicted by the average-particle model.

Figure 12(b) presents the local volume-averaged reaction rate predicted by the two models. The transition

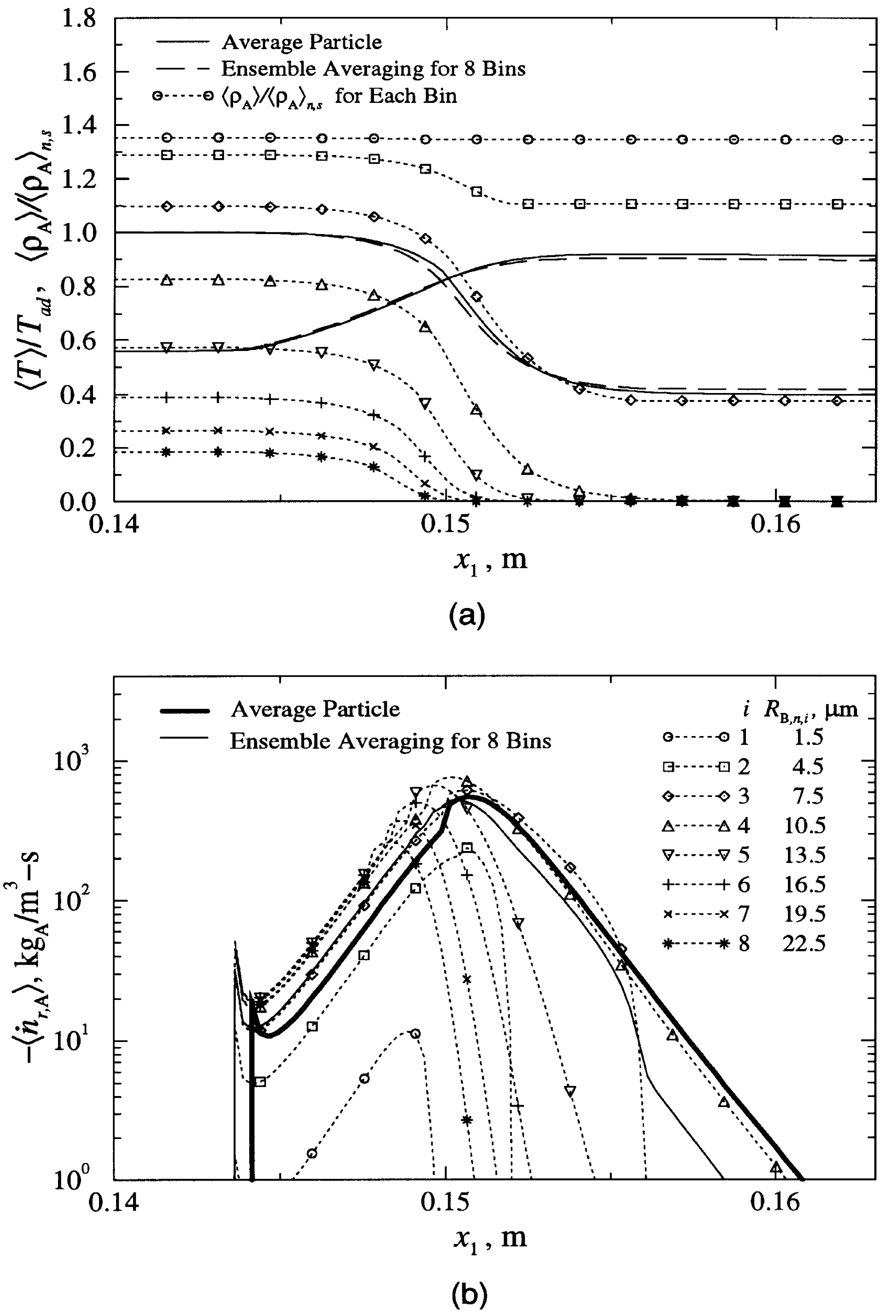

Fig. 12. Effect of the particle size distribution on the local volume-averaged reaction rate. (a) Local volume-averaged temperature and species A concentration distributions, and (b) local volume-averaged reaction rates predicted by the average-particle model and the distributed particle model.

from the primary-diffusion regime to the secondary-diffusion regime occurs at different values of x_1 for each bin. Thus, the local volume-averaged reaction rate for the distributed-particle model does not present the sharp transition that exists for the average particle model. The peak reaction rate does not change appreciably from one model to the other (after D_o is corrected). The reaction rate for the subunit cells initially increases with the species B particle size due to the increase in the surface area of the particle (where the reaction takes place). Then, in the primary-diffusion regime, the reaction rate decreases due to the increase in the thickness of the diffusion layer. In the secondary-diffusion regime, it decreases mainly due to the consumption of species A. The distributed-particle model results in a smaller reaction-region thickness, characterized by a sudden decrease in the reaction rate. This sharp decrease is related to the consumption of the particle class with the greater probability (bin number 3). The only particle bin that continues to react after the flame front is passed is bin number 4, which presents a behavior approximately equal to the average particle size ($\overline{R_{\mathrm{B,n}}} = 8.5$ μm).

5.4. Role of average particle size

Figure 13 presents the variation of the flame speed and the reaction temperature (peak temperature reached in the combustion region) with respect to the average particle radius of species B. The conversion fraction F_c has been kept constant for all the average particle sizes. This corresponds to keeping the shape parameter b constant and changing the scale parameter θ in order to obtain the desired average particle radius $\overline{R_{\mathrm{B,n}}}$ (a change in θ displaces the distribution function along the axis $R_{\mathrm{B,n}}$). The experimental results for the two different average particle radii are also shown. Note that the model has been curve fitted to the experimental results for $\overline{R_{\mathrm{B,n}}} = 8.5$ μm and its behavior follows the behavior exhibited by the other average particle radius. The model predicts extinguishment for average particle radii larger than 14 μm. The flammability limit can be increased to larger average particle radii, if the standard deviation of the particle-size distribution function is decreased, for example, through the proper screening of the powders (which would lead to a larger value of b). In the limit of a uniform particle-size distribution (zero standard deviation), the maximum flammability limit, for the binary system used (and for the external heat loss and volume/surface area conditions), is achieved. For small values of $\overline{R_{\mathrm{B,n}}}$, the reaction becomes surface-kinetic controlled. This chemical kinetic-controlled regime, for the powders commonly used in combustion synthesis, occurs for very small particles (usually smaller than those available commercially). In Fig. 13, the dashed line represents this extrapolated chemical kinetic-controlled regime. For small values of $\overline{R_{\mathrm{B,n}}}$, but yet in the diffusion-controlled regime, solutions obtained using the thin-flame asymptotic (e.g. Armstrong [19]) can be used to predict the propagation speed, if one

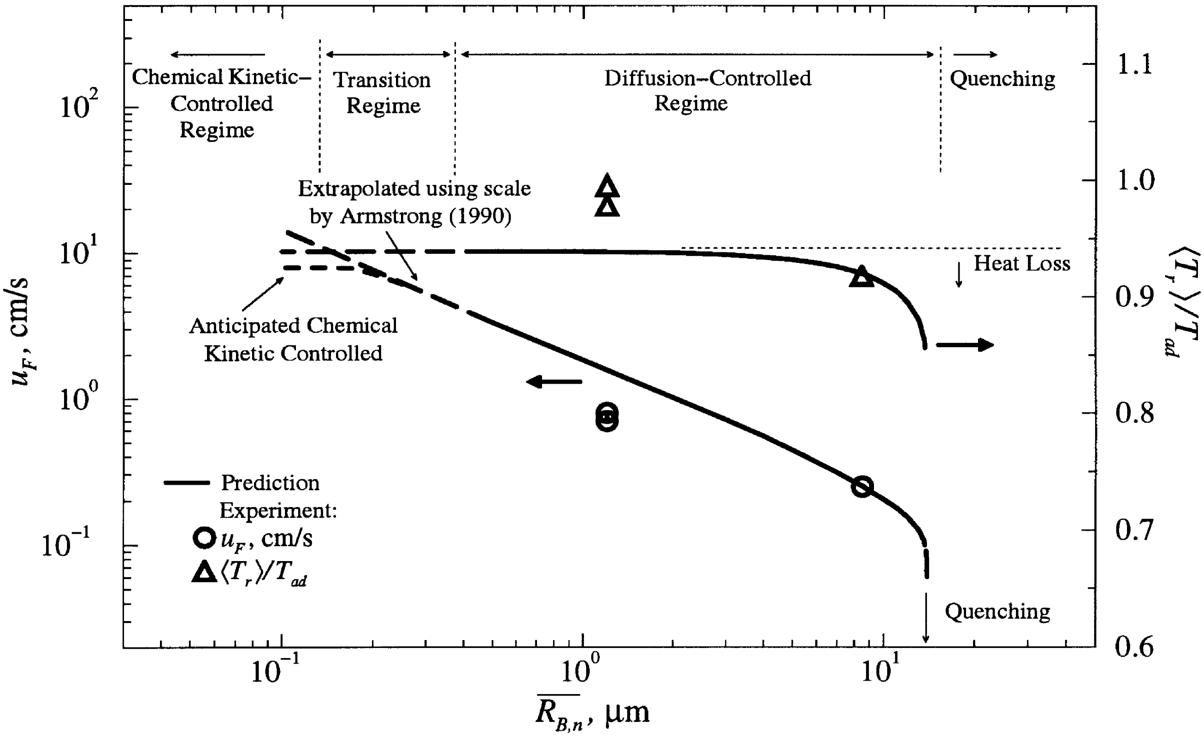

Fig. 13. The variations of combustion front speed u_F and the normalized peak temperature in the combustion region $\langle T_r \rangle / T_{\max}$, with respect to the average titanium particle radius $\overline{R_{\mathrm{B,n}}}$ for the conversion fraction $F_c = 0.602$ (corresponding to $b = 2.7$).

experimental value is available (and using the appropriate T_r). The heat loss to the ambient has a small effect on the peak temperature in the combustion region T_r, for small values of $\overline{R_{B,n}}$. As $\overline{R_{B,n}}$ becomes large, this effect becomes more pronounced and finally is responsible for the extinguishment.

6. Conclusions

A three-scale, particle-level/specimen-level treatment is applied to the gasless compacted-powder combustion synthesis. The specimen-level treatment is based on the local volume-averaged equations for species and energy. The particle-level treatment includes the intraparticle and interparticle diffusion. The intraparticle-diffusion model assumes that the product formation is through a diffusion-controlled heterogeneous reaction at the surface of the high melting temperature reactant. The diffusion is modeled with two regimes, a primary-diffusion regime followed by a slower secondary-diffusion regime. Melting of the product is characterized by a diffusion-controlled regime followed by an energy-controlled regime.

The interparticle-diffusion model determines the amount of reactants available for the reaction. The nonuniform particle size distribution causes a nonuniform local distribution of aluminium and titanium, creating melt-rich and melt-lean regions which limit the conversion of the larger titanium particles. Using a simplified model to account for the local heterogeneity, it was determined that for the powders used, only 46% of the aluminium mass is initially available for conversion to Al_3Ti. This conversion fraction results in a reaction temperature smaller than the one measured. The measurements also show a final conversion fraction of 96%. The secondary-diffusion regime in the intraparticle-diffusion extends the thickness of the reaction region, thus extending the effect of heat loss. The product phase change also extends the reaction region, but, for the system studied, the phase change has a minor role. With these two effects combined, it was determined that the heat losses are responsible for only a 30 K decrease in the maximum temperature. Therefore, the combined effects of intraparticle diffusion and phase change alone do not seem to be able to explain the lower reaction temperatures and the extensive conversion observed experimentally. The low reaction temperature and extensive conversion seem to indicate that the amount of aluminium initially available for reaction is smaller than the stoichiometric mass of aluminium but aluminium migration occurs during the combustion process until the temperature drop does not allow for the liquid migration. This interparticle-diffusion process may become the rate-controlling process for the post reaction-front region. The simultaneous inter- and intraparticle diffusion effects, may explain the 'burn-out' phenomenon reported in the literature (Armstrong [20]).

The importance of the product melting in the redistribution of heat in the combustion region increases for systems in which there is an appreciable formation of liquid product, e.g., Al–Ni. For these systems, the large amount of liquid produced may flow through the solid matrix or cause structural destabilization. Additional details about the model and the results can be found in [27].

The conversion to the final product may be preceded by the formation of intermediate compounds, as observed experimentally for some systems (e.g., Al–Ti and Al–Ni [16, 24]). The formation of compounds at the particle-level depends on the thermodynamic properties of the components and on the atomic diffusion at the interfaces. For the Al–Ti system, at the composition correspondent to $TiAl_3$, there is formation of Ti_3Al and possibly TiAl in the large particles towards the end of the reaction region. At the specimen-level stoichiometries corresponding to TiAl and Ti_3Al, there is extensive formation of intermediate compounds before the final compound is formed [24]. These observations indicate that the models based on the critical gradient $(\nabla c)_c$ concept might be able to predict the compound formation during the combustion synthesis [25, 26].

Here we did not attempt to model the resistance for the interparticle diffusion (it is assumed to be very large). We plan to include this resistance and combine it with the intraparticle diffusion in the secondary-diffusion regime. This would extend the secondary-diffusion regime to include the cool-down up to the solidification temperature of the low-temperature reactant.

Acknowledgements

The financial support of the Conselho Nacional de Desenvolvimento Científico e Technológico—CNPq, Brazil, and the US National Science Foundation are appreciated. Brian D'Amico and Gustavo Freitag have assisted in the experiments and their contributions are greatly appreciated.

References

[1] A.A.M. Oliveira, M. Kaviany, Role of inter- and intraparticle diffusion in nonuniform particle size gasless compacted-powder combustion synthesis—I: formulation, International Journal Heat Mass Transfer 42 (1999) 1059–1073.

[2] H.Y. Sohn, X. Wang, Self-propagating high temperature synthesis (SHS) of intermetallic compounds titanium and nickel aluminides, Materials and Manufacturing Processes 9 (1992) 75–87.

[3] R.N. Wright, B.H. Rabin, W.H. McFerran, Combustion synthesis of cubic Al_3Ti alloys, Journal Material Research 7 (1992) 2733–2738.

[4] K. Hanamura, Private communication, Gifu University, Yanagido, Japan, 1996.

[5] M. Yamaguchi, H. Inui, Al_3Ti and its $L1_2$ variations, in: J.H. Westbrook, R.L. Fleischer (Eds.), Intermetallic Compounds: Vol. 2, Practice. Wiley, New York, 1994. pp. 147–173.

[6] R.B. Banks, Growth and Diffusion Phenomena, Mathematical Frameworks and Applications. Springer-Verlag, New York, 1994. pp. 156–162.

[7] O. Kubaschewski, E.L. Evans, Metallurgical Thermochemistry, 2nd ed., Wiley, New York, 1956.

[8] O. Kubaschewski, C.B. Alcock, Metallurgical Thermochemistry, 5th ed., Pergamon Press, Oxford, 1977.

[9] R. Hultgren, R.L. Orr, P.D. Anderson, K.K. Kelley, Selected Values of Thermodynamic Properties of Metals and Alloys. Wiley, New York, 1963.

[10] O. Kubaschewski, C.B. Alcock, P.J. Spencer, Materials Thermochemistry, 6th ed., Pergamon Press, Oxford, 1993.

[11] J. Zou, C.-L. Fu, M.-H. Yoo, Phase stability of intermetallics in the Al–Ti system: a first principles total-energy investigation, Intermetallics 3 (1995) 265–269.

[12] G.R. Hadley, Thermal conductivity of packed metal powders, International Journal Heat Mass Transfer 29 (1986) 909–920.

[13] W. Sprengel, N. Oikawa, H. Nakajima, Single-phase interdiffusion in TiAl, Intermetallics 4 (1996) 185–189.

[14] E.S. Machlin, An Introduction to Aspects of Thermodynamics and Kinetics Relevant to Materials Science, Giro Press, Croton-on-Hudson, NY, 1991.

[15] S.V. Patankar, Numerical Heat Transfer and Fluid Flow, Hemisphere Publishing Co., Washington, DC, 1980.

[16] D.E. Alman, J.A. Hawk, A.V. Petty, J.C. Rawers, Processing intermetallic composites by self-propagating, high temperature synthesis, Journal of Metals, March 1994, 31–35.

[17] H.G. Kaper, G.K. Leaf, S.B. Margolis, B.J. Matkowski, On nonadiabatic condensed phase combustion, Combust. Sci. Tech. 53 (1987) 289–314.

[18] A.P. Hardt, P.V. Phung, Propagation of gasless reactions in solids—I. Analytical study of exothermic intermetallic reaction rates, Combust. Flame 21 (1973) 77–89.

[19] R. Armstrong, Models for gasless combustion in layered materials and random media, Combust. Sci. Tech. 71 (1990) 155–174.

[20] R. Armstrong, Theoretical models for the combustion of alloyable materials, Metallurgical Transactions A 23A (1992) 2339–2347.

[21] Y. Zhang, G.C. Stangle, A micromechanistic model of the combustion synthesis process: II Numerical simulation, J. Mater. Res. 9 (1994) 2605–2619.

[22] A.P. Aldushin, T.M. Martem'yanova, A.G. Merzhanov, B.I. Khaikin, K.G. Shkadinskii, Propagation of the front of an exothermic reaction in condensed mixtures with the interaction of the components through a layer of high-melting product, Comb. Exp. Shock Waves 8 (1972) 159–167.

[23] S.D. Dunmead, Z. Munir, Temperature profile analysis in combustion synthesis: I, theory and background, J. Am. Ceramic Soc. 75 (1992) 175–179.

[24] C.R. Kachelmyer, J.-P. Lebrat, A. Varma, P.J. McGinn, Combustion synthesis of intermetallic aluminides: processing and mechanistic studies, in: B. Farouk, M. Pinar Menguc, R. Viskanta, C. Presser, S. Chellaiah. Heat Transfer in Fire and Combustion Systems, ASME HTD-Vol 250, New York, 1993, pp. 271–276.

[25] J.J. Hoyt, L.N. Brush, On the nucleation of an intermediate phase at an interface in the presence of a concentration gradient, J. Appl. Phys. 78 (1995) 1589–1594.

[26] F. Hodaj, P.J. Desré, Effect of a sharp gradient of concentration on nucleation of intermetallics at interfaces between polycrystalline layers, Acta Materialia 44 (1996) 4485–4490.

[27] A.A.M. Oliveira, Effect of particle- and specimen-level transport on product state in compacted-powder combustion synthesis and thermal debinding of polymers from molded powders, Ph.D. thesis, The University of Michigan, Ann Arbor, MI, 1998.